Dopant low-n Rydberg states in CF_4 and CH_4 near the critical point

Luxi Li [a,b], Xianbo Shi [a,b], G. L. Findley [c], C. M. Evans [a,b,*]

[a] *Department of Chemistry and Biochemistry, Queens College – CUNY, Flushing, NY 11367, United States*

[b] *Department of Chemistry, Graduate Center – CUNY, New York, NY 10016, United States*

[c] *Department of Chemistry, University of Louisiana at Monroe, Monroe, LA 71209, United States*

Abstract

Dopant low-n Rydberg states perturbed by dense CF_4 and CH_4 were investigated using vacuum ultraviolet photoabsorption spectroscopy at noncritical temperatures and on an isotherm near (+0.5°C) the perturber critical temperature. A full analysis of these data using semi-classical line shape theory was performed. The perturber-induced energy shift was extracted from the simulated bands and demonstrates a perturber critical point effect on the energy of low-n Rydberg states in these molecular fluids.

Key words: VUV absorption, methyl iodide, xenon, critical point effect, low-n Rydberg states

* Corresponding author.
Email addresses: lu.li@qc.cuny.edu (Luxi Li), xianbo.shi@qc.cuny.edu

1 Introduction

Because of the extreme sensitivity of Rydberg states to their environment, these states make excellent spectroscopic probes of both external fields and perturber media [1,2]. In fact, dopant low-n Rydberg states [3–13] have been used to investigate solvation effects in atomic and molecular fluids, albeit none of these earlier studies [3–13] has probed temperature effects in near critical point fluids across a broad density range. (Larrégaray, *et al.* [12], however, did report a change in the argon induced energy shift and in the fluorescence line shape for the X $^2\Pi(\nu = 0) \leftarrow$ A $^2\Sigma^+(\nu' = 0)$ nitric oxide transition at the critical density of argon.)

Recently, we have measured photoabsorption spectra of dopant low-n Rydberg states [14–16] in the rare gas perturbers Ar, Kr and Xe. As expected, these studies showed that the dopant low-n Rydberg states shift and broaden significantly as the perturber number density increases from low density to the density of the triple point liquid. However, we also demonstrated that a semi-classical statistical line shape analysis [14–16] adequately simulates the experimental absorption spectra at noncritical temperatures and on an isotherm near the critical isotherm of the perturber. The perturber induced energy shift $\Delta(\rho_{\rm P})$ was obtained from a standard moment analysis of the simulated transitions, and showed a striking critical point effect near the critical temperature and density of the perturbers [14–16].

In this Letter, we extend these measurements and analyses to selected molec-

(Xianbo Shi), findley@ulm.edu (G. L. Findley), cherice.evans@qc.cuny.edu (C. M. Evans).

ular fluids. We present absorption spectra of the xenon $6s$ Rydberg state perturbed by CF_4, and of the CH_3I $6s$ state perturbed both by CF_4 and by CH_4. (The CH_3I $6s'$ state was also investigated [16] and showed a behavior similar to that of the $6s$ state. For the sake of brevity, these results are not presented here.) Each dopant/perturber system was studied from low perturber number density to the density of the triple point liquid, at noncritical temperatures and on an isotherm near (i.e., +0.5°C) the critical isotherm of the perturber. We show that the semi-classical line shape theory previously used to model low-n Rydberg states in atomic fluids [14–16] successfully simulates our current experimental results. A moment analysis of the simulated primary transition exhibits a distinct critical point effect comparable to that observed in the rare gas perturbers [14–16]. Finally, the importance of including three-body interactions in the line shape analysis is investigated.

2 Experiment

Details of the photoabsorption measurements have been provided previously [14–16]. Briefly, monochromatic synchrotron radiation having a resolution of 10 meV in the spectral range of interest was transmitted through a copper cell equipped with MgF_2 windows. This sample cell, which can withstand pressures of up to 100 bar, was attached to an open flow liquid nitrogen cryostat and resistive heater that allowed the temperature to be maintained to ±0.5°C at noncritical temperatures and to ±0.2°C near the critical isotherm. The set point for the critical isotherm was chosen to be 0.5°C above the perturber critical temperature (i.e., $T_c = -45.7$°C for CF_4 [17–20] and −82.1°C for CH_4 [21]) in order to prevent liquid formation in the cell during tempera-

ture stabilization. The pressure and temperature of the sample were used to determine the number density of the perturber from the relevant empirical equation of state: For carbon tetrafluoride we used the Benedict-Webb-Rubin equation of state [17] for $T \geq T_c$ and a Peng-Robinson equation of state [18] for $T < T_c$ with parameters from [19,20]; a modified Benedict-Webb-Rubin equation of state [21] was used for methane. The dopant concentration was optimized for each perturber number density, but was kept under 10 ppm for all dopant/perturber samples measured.

Xe (Matheson Tri-gas Inc., 99.995%), CH_3I (Aldrich, 99.45%), CF_4 (Matheson Tri-gas Inc., 99.999%) and CH_4 (Matheson Tri-gas Inc., 99.999%) were used without further purification. The absence of trace impurities in the spectral region of interest was verified from the measured transmission spectra. (The transmission spectrum of high density CF_4 indicated a small N_2 impurity at energies greater than 8.6 eV, which precluded the investigation of the Xe $6s'$ Rydberg state in CF_4. The strong absorption of CH_4 at energies greater than 8.4 eV prevented the measurement of both the Xe $6s$ and $6s'$ Rydberg states in methane.) All transmission spectra were normalized both to the incident light intensity and to the empty cell transmission. Once corrected, these spectra were converted to absorbance and normalized to one, in order to allow for comparison with the simulated line shapes. (We should note here, however, that the integrated intensities of the absorption bands prior to normalization are independent of the perturber number density for a given amount of dopant.)

The gas handling system (GHS) and the mixing procedures used to ensure a homogeneous sample have been described previously [16]. The GHS was initially baked to a base pressure of low 10^{-8} Torr. After the addition of a

dopant, the GHS was allowed to return to the low 10^{-7} Torr range before the introduction of the perturber. The GHS was baked to a base pressure of low 10^{-8} Torr before switching to a different dopant/perturber system, which prevented cross-contamination.

3 Simulations

The experimental line shapes were simulated using a semi-classical approximation, given as a Fourier transform [3,4,10,14–16]

$$\mathfrak{L}(\omega) \;=\; \frac{1}{2\,\pi}\,\mathrm{Re}\int_{-\infty}^{\infty} dt\;\mathrm{e}^{-i\,\omega\,t}\;\langle \mathrm{e}^{i\,\omega(\mathbf{R})\,t}\,\rangle\;, \tag{1}$$

where $\langle\cdots\rangle$ represents the thermal average; $\mathbf{R}$ denotes the collection of all dopant/perturber distances; $\omega \;=\; \omega(\mathbf{R}) - \omega_0$, with ω_0 being the transition frequency for the neat dopant; and t is the reduced time (i.e., time divided by $\hbar$, the reduced Planck constant). Eq. (1) neglects lifetime broadening and assumes that the transition dipole moment is independent of $\mathbf{R}$. When an exponential density expansion is performed on $\langle \mathrm{e}^{i\,\omega(\mathbf{R})\,t}\,\rangle$ under the assumption that only two-body and three-body interactions contribute to the line shape, eq. (1) becomes [3,4,10,14–16]

$$\mathfrak{L}(\omega) \;=\; \frac{1}{2\,\pi}\,\mathrm{Re}\int_{-\infty}^{\infty} dt\;\mathrm{e}^{-\,i\,\omega\,t}\;\exp\left[A_1(t)\;+\;A_2(t)\right] \quad . \tag{2}$$

The contribution $A_1(t)$ to $\mathfrak{L}(\omega)$ from two-body interactions is determined from [3,4,10,14–16]

$$A_1(t) \;=\; 4\,\pi\,\rho_{\mathrm{P}}\int_0^{\infty} dr\;r^2\;g_{\mathrm{PD}}(r)\left[\;\mathrm{e}^{-\,i\,t\,\Delta V(r)}\;-\;1\;\right] \quad , \tag{3}$$

while $A_2(t)$, which represents the contribution from three-body interactions, is approximated by [3,4,10,14–16]

$$\begin{aligned} A_2(t) \;=\; & 4\,\pi\,\rho_{\rm P}^2 \int_0^\infty dr_1\; r_1^2\; g_{\rm PD}(r_1)\; \left[{\rm e}^{-\,i\,t\,\Delta V(r_1)} \;-\; 1 \right] \\ & \times \int_0^\infty dr_2\; r_2^2\; g_{\rm PD}(r_2)\; \left[\; {\rm e}^{-\,i\,t\,\Delta V(r_2)} \;-\; 1\;\right] \\ & \times \frac{1}{r_1\; r_2} \int_{|r_1\,-\,r_2|}^{|r_1\,+\,r_2|} s\;[\;g_{\rm PP}(s) \;-\; 1\;]\;ds\;. \end{aligned} \tag{4}$$

In eqs. (3) and (4), $\rho_{\rm P}$ is the perturber number density, $g_{\rm PP}(r)$ is the perturber/perturber radial distribution function, $g_{\rm PD}(r)$ is the ground state dopant/perturber radial distribution function, and $\Delta V(r) = V_e(r) - V_g(r)$, where $V_e(r)$ and $V_g(r)$ are the excited state dopant/perturber and ground state dopant/perturber interaction potentials, respectively. The required radial distribution functions $g_{\rm PP}(r)$ and $g_{\rm PD}(r)$ were obtained from the analytical solution of the Ornstein-Zernike equation for a binary system within the Percus-Yevick (PY) closure [22], while the Fourier transform of $\mathfrak{L}(\omega)$ was performed using a standard fast Fourier transform algorithm [16,23]. The line shape from this transform was convoluted with a Gaussian slit function to account for the finite resolution (10 meV) of the monochromator.

Eqs. (2) – (4) are explicitly dependent on the excited and ground state dopant/perturber intermolecular potentials through $\Delta V(r)$, and are implicitly dependent on the perturber/perturber and ground state dopant/perturber intermolecular potentials via $g_{\rm PP}(r)$ and $g_{\rm PD}(r)$, respectively. Thus, these simulations allow one to determine a single set of ground and excited state intermolecular potential parameters for each system. However, we should note that eqs. (2) – (4) are relatively insensitive to the choice of perturber/perturber intermolecular potential. Therefore, when possible, the perturber/perturber intermolecular potentials were obtained from modeling the quasi-free electron

energy $V_0(\rho_{\rm P})$ in the perturber [24]. The investigation of $V_0(\rho_{\rm P})$ in CH_4 [24,25] substantiated that a two-Yukawa potential,

$$V(r) \;=\; -\,\frac{\kappa_0\,\varepsilon}{r}\left[{\rm e}^{-\,z_1\,(r\,-\,\sigma)} \;-\; {\rm e}^{-\,z_2\,(r\,-\,\sigma)}\right]\,, \tag{5}$$

is suitable for the CH_4/CH_4 interactions. $V_0(\rho_{\rm P})$ in CF_4 from low density to the density of the triple point liquid has not been measured [24]. Therefore, for simplicity, a standard Lennard-Jones 6-12 potential,

$$V(r) \;=\; 4\,\varepsilon\left[\left(\frac{\sigma}{r}\right)^{12} \;-\; \left(\frac{\sigma}{r}\right)^{6}\right]\,, \tag{6}$$

was chosen for the CF_4/CF_4 interactions.

A Lennard-Jones 6-12 intermolecular potential was also selected to model the interaction of ground state Xe with CF_4, since a similar potential was successfully applied in the simulation of Xe low-n Rydberg states in Ar [14,16]. Moreover, the modified Stockmayer potential,

$$V(r) \;=\; 4\,\varepsilon'\left[\left(\frac{\sigma'}{r}\right)^{12} \;-\; \left(\frac{\sigma'}{r}\right)^{6}\right] \;-\; \frac{1}{r^6}\alpha_{P}{\mu_{D}}^{2}\,, \tag{7}$$

was chosen for the CH_3I/molecular perturber interactions because line shape simulations [15,16] of CH_3I in Ar, Kr and Xe showed that this potential adequately modeled the interaction of dilute CH_3I with these atomic fluids. (One should note that the modified Stockmayer potential includes orientational effects via an angle average that presumes the free rotation of CH_3I [26].) The modified Stockmayer potential can be rewritten in standard Lennard-Jones 6-12 form [26], with the parameters

$$\varepsilon = \varepsilon'\left[1 + \alpha_{P}{\mu_{D}}^{2}/(4\varepsilon'{\sigma'}^{6})\right]^{2}$$

and

$$\sigma = \sigma'\left[1 + \alpha_{P}{\mu_{D}}^{2}/(4\varepsilon'{\sigma'}^{6})\right]^{-1/6}\;.$$

Finally, all of the excited state dopant/ground state perturber interactions were treated with an exponential-6 potential,

$$V(r) \;=\; \frac{\varepsilon}{1-(6/\gamma)} \left\{ \frac{6}{\gamma}\, e^{\gamma(1-\chi)} - \chi^{-6} \right\} , \tag{8}$$

which was used previously [14–16] in our studies of dopant low-n Rydberg states in Ar, Kr and Xe. In eqs. (6) - (8), ε (or ε') is the well-depth, σ (or σ') is the collision parameter, α_P is the perturber polarizability, μ_D is the dopant dipole moment, $\chi \equiv r/r_e$ (where r_e is the equilibrium distance), κ_0, z_1, z_2, are collision parameters and γ is the potential steepness. All dopant/perturber parameters (and the CF_4/CF_4 parameters) were adjusted by hand in a consistent manner to give the best simulated line shape in comparison to experiment from low perturber density to the density of the triple point liquid, at noncritical temperatures and on an isotherm near the critical isotherm.

4 Results and discussion

Selected absorption spectra (solid lines) for the Xe $6s$ Rydberg state are presented in Fig. 1 for noncritical temperatures and on an isotherm near the CF_4 critical isotherm. These spectra, which are offset vertically by the CF_4 number density, show a single band that both broadens to the blue and blue shifts as a function of perturber density. The Xe $6s$ Rydberg state doped into Ar, on the other hand, possessed two blue satellite bands that were attributed to the formation of ground and excited state Xe/Ar dimers [3,14,16]. The absence of these higher energy bands in the absorption spectra shown in Fig. 1 indicates that Xe/CF_4 dimers do not interfere. The presence of a single transition implies that a moment analysis of the experimental data should yield

the perturber-induced energy shift of the Xe $6s$ transition. However, at higher CF_4 number densities, the absorption of the nitrogen impurity becomes apparent. As the nitrogen peaks begin to grow into the absorption spectrum, these transitions distort the CF_4 broadened Xe $6s$ band and prevent an accurate determination of the band energy from a standard moment analysis at high density. A moment analysis on the simulated line shape of the primary Xe transition

$$\mathrm{Xe} + h\nu \quad \xrightarrow{\mathrm{CF_4}} \quad \mathrm{Xe}^* \,,$$

however, can be used to determine $\Delta(\rho_{\mathrm{CF_4}})$, if the simulations adequately match the experimental data in Fig. 1.

Figs. 2 and 3 show selected absorption spectra (solid lines), again offset vertically by the perturber number density, for the CH_3I $6s$ Rydberg state in CF_4 and CH_4, respectively. Two distinct bands are clearly observed in the lower number density spectra. The lower energy band represents the adiabatic transition [15]

$$\mathrm{CH_3I} + \ h\nu \quad \xrightarrow{\mathrm{P}} \quad \mathrm{CH_3I}^* \,,$$

while the higher energy band represents one quantum of the CH_3 deformation vibrational transition ν_2 in the excited state [15]

$$\mathrm{CH_3I} + \ h\nu \quad \xrightarrow{\mathrm{P}} \quad \mathrm{CH_3I}^* \ (\nu_2) \,.$$

Since both of these bands independently blue broaden and blue shift as a function of perturber density and, in fact, merge at higher perturber number densities, determining $\Delta(\rho_{\mathrm{CH_4}})$ for the adiabatic transition is impossible. Therefore, any line shape simulation that accurately reproduces experiment must include both transitions. Once this simulation is performed, the perturber induced shift $\Delta(\rho_{\mathrm{CH_4}})$ can be calculated from a moment analysis of the

simulated adiabatic transition.

The dotted lines in Figs. 1 – 3 represent the simulations that gave the best fit to experiment, for the intermolecular potential parameters given in Table 1. For CH_3I, the relative intensities of the adiabatic and vibrational bands were fixed by comparison to the absorption spectra at perturber number densities where both bands could be clearly identified. The ratio of the vibrational band intensity to the adiabatic transition intensity was held at 0.22 for all simulations in both CF_4 and CH_4. Clearly, the simulated spectra closely match the experimental spectra for all three dopant/perturber systems

Given these accurate simulations, the perturber induced shift $\Delta(\rho_{\rm P})$ can be approximated as the first moment [3,4]

$$\Delta(\rho_{\rm P}) \equiv M_1 = \int \mathfrak{L}(E)\, E\, dE \Big/ \int \mathfrak{L}(E)\, dE \tag{9}$$

of the primary (or adiabatic) transition, where $\mathfrak{L}(E)$ is the simulated absorption band and $E = \hbar(\omega - \omega_0)$. These first moments are presented in Fig. 4 as a function of the reduced perturber number density ρ_r (where $\rho_r = \rho/\rho_c$, with $\rho_c \equiv$ critical density). Similar to the behavior observed in atomic fluids [14–16], the first moment shows a perturber induced blue shift from low density to the density of the triple point liquid with a distinct change in $\Delta(\rho_{\rm P})$ near the critical density and temperature of the perturber. The total blue shift is caused by the shielding of the optical electron from the cationic core by the first solvent shell of the perturber. Thus, as the perturber number density increases, the low-n Rydberg state excitation energy shifts toward higher energies. Similarly, near the perturber critical point, the local density of the perturber increases due to stronger dopant/perturber correlations. This local density change, which occurs primarily in the first solvent shell [24], also

increases the perturber induced shielding of the optical electron and, therefore, causes an increase in the blue shift of the low-n Rydberg state excitation energy.

In comparing $\Delta(\rho_{\rm P})$ for CF_4 and CH_4, we note that CF_4 shifts the Rydberg transitions farther to the blue than does CH_4. Following the law of corresponding states, all gases should deviate from ideal behavior to approximately the same degree when reduced variables are used. Since CH_4 and CF_4 are highly symmetric, the reduced density at the triple point should be similar. However, although CH_4 has a reduced triple point density that is similar to that of the rare gases (i.e., 2.65 ± 0.05), the reduced triple point density of CF_4 is 3.00. Moreover, the compressibility factor for CF_4 at higher densities is significantly smaller than that for CH_4, indicating that CF_4 is a more attractive gas at higher number densities, leading to a larger local number density around the dopant molecule. This, in turn, yields a larger total blue shift for dopant low-n Rydberg states perturbed by CF_4. Although there is also a significant enhancement of the local density around the dopant in near critical point CF_4, this enhancement does not yield a large critical point effect in $\Delta(\rho_{\rm CF_4})$ because of the low bulk critical density of 4.3×10^{21} cm^{-3}.

The CH_3I/CH_4 system shows a critical point effect that is larger than that in CH_3I/CF_4, as well as being larger than those [14–16] in CH_3I/Ar, CH_3I/Kr and CH_3I/Xe. This variation is caused by the strength of the CH_3I/perturber interactions in comparison to the perturber/perturber interactions, coupled with the differences in the ground and excited state dopant/perturber intermolecular potentials. The CH_3I/CH_4 well depth is close (i.e., to within 54 K) to the CH_4/CH_4 well depth. This implies that the CH_3I/CH_4 interactions near the CH_4 critical point will be comparable to the CH_4/CH_4 interactions. Thus,

one would expect a larger increase in the local perturber density near the critical point of the perturber, implying a larger critical point effect. However, the similarities between the CH_3I/CH_4 and CH_4/CH_4 interactions are not as strong as those reported for the CH_3I/Kr and Kr/Kr interactions [15,16], although the critical point effect observed in CH_4 is 20 meV larger than that for Kr. This larger effect in CH_3I/CH_4 is due to the fact that the excited state CH_3I/CH_4 interaction is also comparable to the ground state CH_4/CH_4 interaction. (The well depth for the CH_3I $6s/CH_4$ potential is only 5 K different from that for the CH_4/CH_4 potential, whereas the well depth for the CH_3I $6s$/Kr interaction is 72 K different from that for the Kr/Kr interaction.) Thus, both ground and excited state CH_3I are strongly stabilized in near critical point CH_4.

In the line shape simulations presented in Figs. 1 – 3, the density expansion of the autocorrelation function was truncated to the second term (i.e., all interactions except two-body and three-body interactions were neglected). Egorov *et al.* [10] simulated the CH_3I $6s$ Rydberg state doped into low density Ar with the density expansion truncated to $A_1(t)$. However, they assumed that the three-body correlation (i.e., $A_2(t)$) would be necessary to model line shapes at higher perturber number densities. The accurate intermolecular potentials obtained here allow us to investigate the truncation of the density expansion in a more detailed manner. We have chosen to consider this for the CH_3I $6s$ Rydberg state perturbed by CH_4, because the broadening and critical point effects are most pronounced there. Fig. 5 presents selected simulated line shapes with the density expansion truncated to the first term $A_1(t)$ (dotted lines) and to the second term $A_2(t)$ (solid lines) both at noncritical temperatures and densities (i–iii) and near the critical point (iv). For the simulations at non-

critical temperatures, the line shapes obtained after truncation to $A_1(t)$ are clearly identical to those obtained when both $A_1(t)$ and $A_2(t)$ are included in eq. (2), even at higher perturber number densities. However, near the perturber critical point, the simulated line shape containing both two-body and three-body interactions is broader than that obtained under the assumption of only two-body interactions. Thus, the increasing correlation lengths of the dopant/perturber and perturber/perturber interactions near the critical point necessitate the inclusion of $A_2(t)$ in order to model accurately the dopant absorption line shape. As originally predicted by Messing *et al.* [3,4], however, the perturber-induced energy shift $\Delta(\rho_{\mathrm{P}})$ depends only on two-body interactions (cf. Fig. 6), even along the critical isotherm.

In summary, we have presented absorption spectra of dopant low-n Rydberg states in varying number densities of CF_4 and CH_4. An appropriate choice of intermolecular potentials permitted an accurate simulation of the experimental bands at all densities and temperatures. The perturber induced energy shifts $\Delta(\rho_{\mathrm{P}})$ of low-n Rydberg states in CF_4 and CH_4 behaved similarly to those [14–16] observed in Ar, Kr and Xe. However, the large compressiblity of CF_4 led to a larger than expected total blue shift, while the strong ground state and excited state CH_3I/CH_4 interactions yielded the largest critical point effect we have yet observed. Finally, we showed that two-body interactions are sufficient to model the dopant absorption line shapes, except near the perturber critical point, and that these interactions are sufficient to model the energy shift even at the critical point.

Acknowledgements

All experimental measurements were made at the University of Wisconsin Synchrotron Radiation Center (NSF DMR-0537588), with support from the Petroleum Research Fund (PRF#45728-B6), the Professional Staff Congress - City University of New York and the Louisiana Board of Regents Support Fund (LEQSF(2006-09)-RD-A-33).

References

[1] T. F. Gallagher, Rydberg Atoms, Cambridge University Press, Cambridge, 2005, and references therein.

[2] M. B. Robin, Higher Excited States of Polyatomic Molecules, vols. I–III, Academic Press, New York, 1974, 1975, 1985, and references therein.

[3] I. Messing, B. Raz, J. Jortner, J. Chem. Phys. 66 (1977) 2239 , and references therein.

[4] I. Messing, B. Raz, J. Jortner, J. Chem. Phys. 66 (1977) 4577.

[5] I. Messing, B. Raz, J. Jortner, Chem. Phys. 25 (1977) 55.

[6] I. Messing, B. Raz, J. Jortner, Chem. Phys. 23 (1977) 351.

[7] T. Kalbfleisch, R. Fan, P. Moore, L.D. Ziegler, J. Chem. Phys. 103 (1995) 7673.

[8] R. Fan, T. Kalbfleisch, L.D. Ziegler, J. Chem. Phys. 104 (1996) 3886.

[9] T. S. Kalbfleisch, L. D. Ziegler, T. Keyes, J. Chem. Phys. 105 (1996) 7034.

[10] S.A. Egorov, M.D. Stephens, J.L. Skinner, J. Chem. Phys. 107 (1997) 10485.

[11] E. Morikawa, A. M. Köhler, R. Reininger, V. Saile, P. Laporte, J. Chem. Phys. 89 (1988) 2729.

[12] P. Larregaray, A. Cavina, M. Chergui, Chem. Phys. 308 (2005) 13.

[13] C. N. Tiftickjian, S. A. Egorov, J. Chem. Phys. 128 (2008) 114501.

[14] Luxi Li, Xianbo Shi, C. M. Evans, G. L. Findley, Chem. Phys. Lett. 461 (2008) 207.

[15] Luxi Li, Xianbo Shi, C. M. Evans, G. L. Findley, Chem. Phys. 360 (2009) 7.

[16] Luxi Li, Ph.D. dissertation, The Graduate Center of the City University of New York, New York, 2009.

[17] T. E. Morsy, J. Chem. Eng. Data 15 (1970) 256.

[18] H. Orbey, S. I. Sandler, Ind. Eng. Chem. Res. 34 (1995) 2520.

[19] N. B. Wilding, Phys. Rev. E 52 (1995) 602.

[20] J. M. Caillol, J. Chem. Phys. 109 (1998) 4885.

[21] B. A. Younglove, J. F. Ely, J. Phys. Chem. Ref. Data 16 (1987) 577.

[22] E.W. Grundke, D. Henderson, R.D. Murphy, Can. J. Phys. 51 (1973) 1216.

[23] W.H. Press, S.A. Teukolsky, W.T. Vetterling, and B.P. Flannery, Numerical Recipes in FORTRAN: the art of scientific computing, Cambridge University Press, New York, 1992.

[24] Xianbo Shi, Ph.D. dissertation, The Graduate Center of the City University of New York, New York, 2009.

[25] Xianbo Shi, Luxi Li, C. M. Evans, G. L. Findley, Chem. Phys. Lett. (2009) submitted.

[26] J. O. Hirschfelder, C. F. Curtiss, R. B. Bird, Molecular Theory of Gases and Liquids, Wiley, New York, 1954.

Table 1
Intermolecular potential parameters.

	$\varepsilon/k_{\mathrm{B}}$ (K)	r_e (Å)	γ
CF_4/CF_4	181 ± 2	4.71 ± 0.03^a	–
CH_4/CH_4^b	141.5 ± 0.3	3.704 ± 0.005^a	–
Xe/CF_4	219 ± 2	4.63 ± 0.03^a	–
CH_3I/CF_4	256 ± 2	5.02 ± 0.03^a	–
CH_3I/CH_4	196 ± 2	4.24 ± 0.03^a	–
Xe $6s/CF_4$	155 ± 5	6.45 ± 0.06	12.15 ± 0.05
CH_3I $6s/CF_4$	185 ± 5	6.84 ± 0.06	12.10 ± 0.05
CH_3I $6s/CH_4$	145 ± 5	6.55 ± 0.06	10.10 ± 0.05
CH_3I $6s$ ν_2/CF_4	135 ± 5	6.84 ± 0.06	11.90 ± 0.05
CH_3I $6s$ ν_2/CH_4	105 ± 5	6.65 ± 0.06	9.95 ± 0.05

[a] For a Lennard-Jones 6-12 potential and a two-Yukawa potential, $\sigma = 2^{-1/6} r_e$.
[b] Two-Yukawa potential with $\kappa_0 = 8.50$ Å, $z_1 = 0.90$ Å^{-1}, and $z_2 = 4.25$ Å^{-1}. Parameters taken from [24,25].

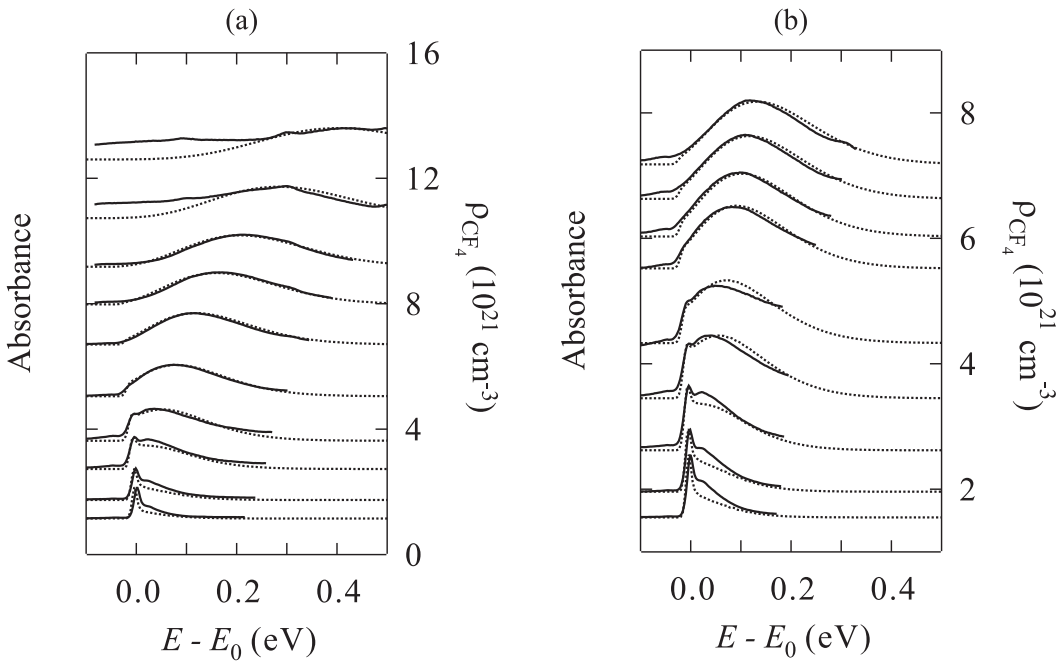

Fig. 1. Selected experimental absorbance (—, relative units) and simulated line shapes ($\cdots$) for the Xe 6*s* Rydberg transition in CF_4 at (a) noncritical temperatures and (b) on an isotherm (-44.9°C) near the critical isotherm. The data are offset vertically by the CF_4 perturber number density ρ_{CF_4}. $E_0 = 8.424$ eV for the unperturbed Xe 6*s* Rydberg transition. (The discrepancies between the experimental and simulated line shapes at the highest densities are due to an N_2 impurity in CF_4.)

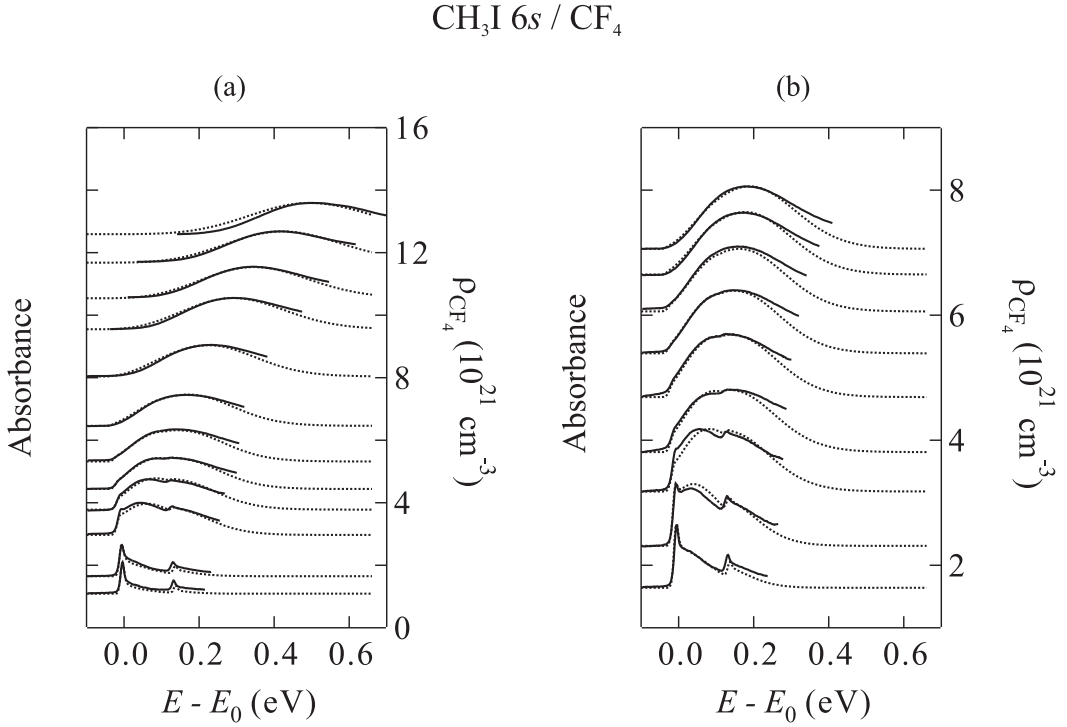

Fig. 2. Selected experimental absorbance (—, relative units) and simulated line shapes ($\cdots$) for the CH_3I 6s Rydberg transition in CF_4 at (a) noncritical temperatures and (b) on an isotherm (-44.9°C) near the critical isotherm. The data are offset vertically by the CF_4 perturber number density ρ_{CF_4}. $E_0 = 6.154$ eV for the unperturbed CH_3I 6s Rydberg transition. (The variation between experiment and simulation on the high energy side is caused by additional vibrational transitions that are not modeled here.)

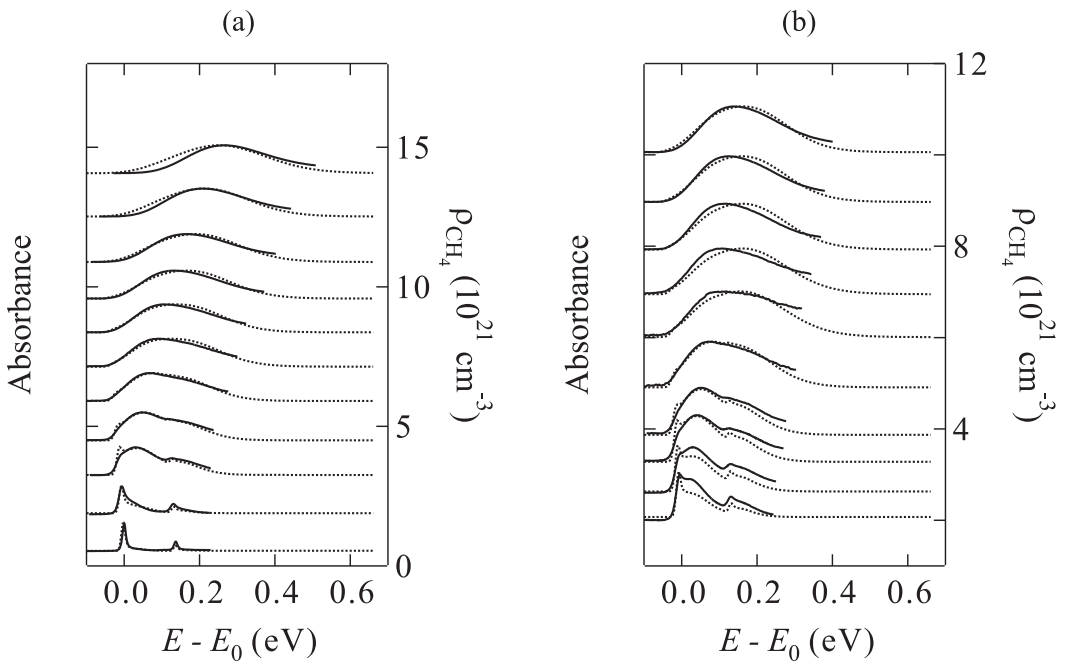

Fig. 3. Select experimental absorbance (—, relative units) and simulated line shapes ($\cdots$) for the CH_3I $6s$ Rydberg transition in CH_4 at (a) noncritical temperatures and (b) on an isotherm (-63.3°C) near the critical isotherm. The data are offset vertically by the CH_4 perturber number density ρ_{CH_4}. $E_0 = 6.154$ eV for the unperturbed CH_3I $6s$ Rydberg transition. (The variation between experiment and simulation on the high energy side is caused by additional vibrational transitions that are not modeled here.)

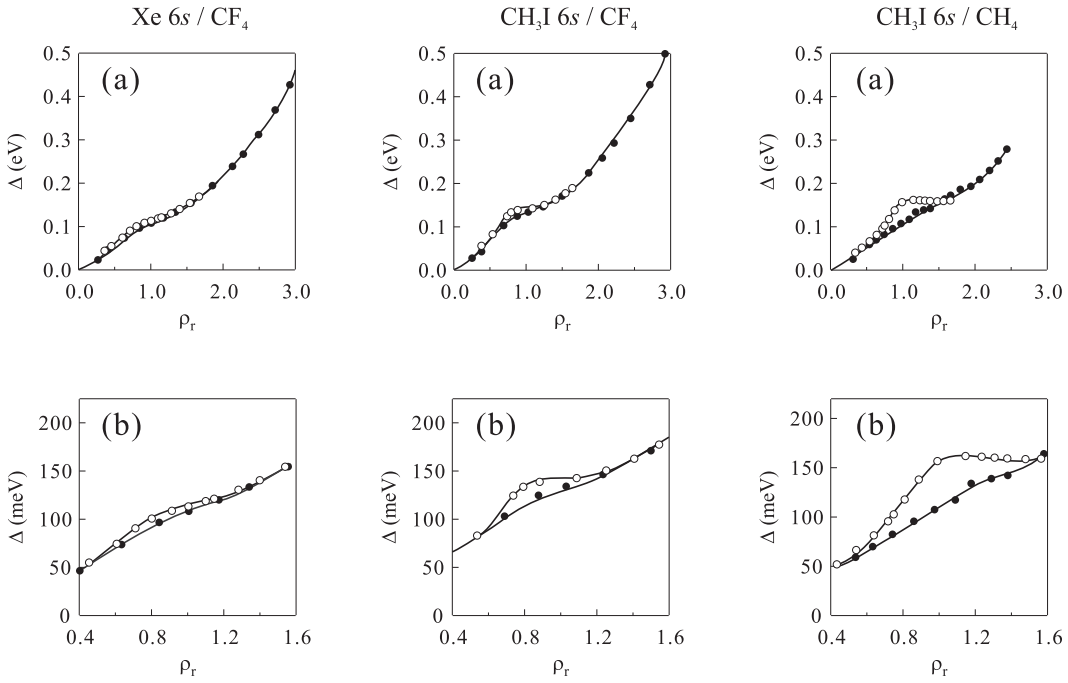

Fig. 4. (a) The perturber induced shift $\Delta(\rho_{\rm P})$, as approximated by a moment analysis, of the simulated primary (or adiabatic) transition for the $6s$ Rydberg states in Xe and CH_3I as a function of the reduced perturber number density ρ_r ($\rho_r = \rho/\rho_c$, $\rho_c \equiv$ perturber critical density). (•), simulations obtained at noncritical temperatures; (◦), simulations near the critical isotherm. (b) An expanded view of $\Delta(\rho_{\rm P})$ near the perturber critical point. $\rho_c = 4.3 \times 10^{21}$ cm^{-3} for CF_4 [17–20] and $\rho_c = 6.1 \times 10^{21}$ cm^{-3} for CH_4 [21]. The solid lines provide a visual aid. See text for discussion.

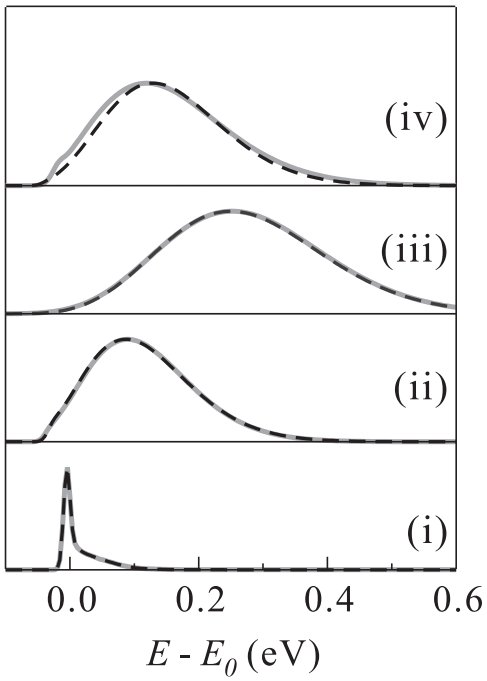

Fig. 5. Comparison of the simulated line shapes for the CH_3I 6s adiabatic Rydberg transition in CH_4 determined from eq. (2) with the density expansion truncated to $A_2(t)$ (grey solid line) and to $A_1(t)$ (black dashed line). Simulations at noncritical temperatures with (i) $T = 25.0°C$ and $\rho = 1.2 \times 10^{21}$ cm^{-3}; with (ii) $T = -70.0°C$ and $\rho = 6.6 \times 10^{21}$ cm^{-3}, which is near the critical density of 6.1×10^{21} cm^{-3}; and with (iii) $T = -143.0°C$ and $\rho = 14.8 \times 10^{21}$ cm^{-3}. (iv) A simulation near the critical point with $T = -81.6°C$ and $\rho = 6.0 \times 10^{21}$ cm^{-3}.

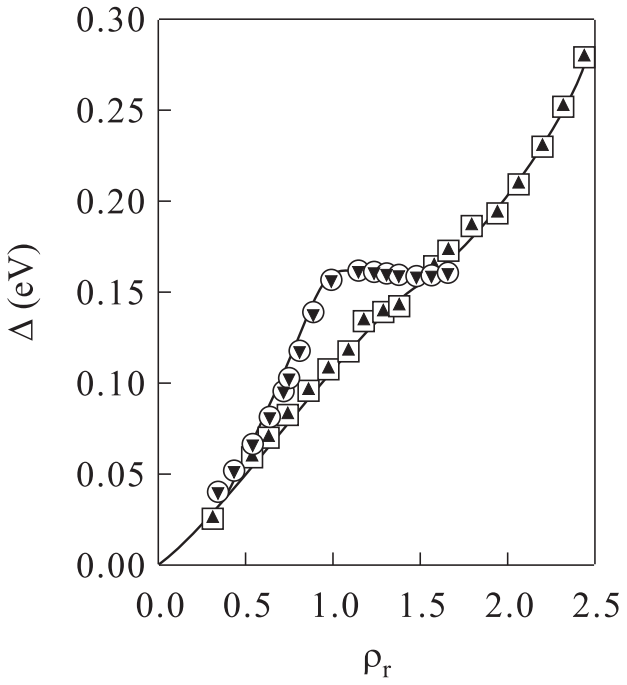

Fig. 6. Comparison of the first moment of the simulated adiabatic transition for CH_3I $6s$ in CH_4. The open and closed markers represent the first moment from simulated line shapes determined with the density expansion truncated to the second term $A_2(t)$ and to the first term $A_1(t)$, respectively. (□,▲) are data obtained at noncritical temperatures, while (∘,▼) are data obtained on an isotherm near the critical isotherm. The solid lines are provided as a visual aid.